X-Ray Luminescence Computed Tomography via Selective Excitation: A Feasibility Study

Guillem Pratx, Colin M. Carpenter, Conroy Sun, and Lei Xing*

Abstract—X-ray luminescence computed tomography (XLCT) is proposed as a new molecular imaging modality based on the selective excitation and optical detection of X-ray-excitable phosphor nanoparticles. These nano-sized particles can be fabricated to emit near-infrared (NIR) light when excited with X-rays, and, because both X-rays and NIR photons propagate long distances in tissue, they are particularly well suited for *in vivo* biomedical imaging. In XLCT, tomographic images are generated by irradiating the subject using a sequence of programmed X-ray beams, while sensitive photo-detectors measure the light diffusing out of the subject. By restricting the X-ray excitation to a single, narrow beam of radiation, the origin of the optical photons can be inferred regardless of where these photons were detected, and how many times they scattered in tissue. This study presents computer simulations exploring the feasibility of imaging small objects with XLCT, such as research animals. The accumulation of 50 nm phosphor nanoparticles in a 2-mm-diameter target can be detected and quantified with subpicomolar sensitivity using less than 1 cGy of radiation dose. Provided sufficient signal-to-noise ratio, the spatial resolution of the system can be made as high as needed by narrowing the beam aperture. In particular, 1 mm spatial resolution was achieved for a 1-mm-wide X-ray beam. By including an X-ray detector in the system, anatomical imaging is performed simultaneously with molecular imaging via standard X-ray computed tomography (CT). The molecular and anatomical images are spatially and temporally co-registered, and, if a single-pixel X-ray detector is used, they have matching spatial resolution.

Index Terms—Molecular imaging, nanophosphor, optical imaging, X-ray computed tomography (CT).

I. INTRODUCTION

CURRENTLY, significant research efforts are focused on improving biomedical imaging by exploiting the unique properties of nanomaterials, such as quantum confinement, which gives quantum dots their wavelength tunability [1], and superparamagnetism, which has been used in magnetic resonance imaging (MRI) contrast agents [2]. In addition, the ability to specifically target biological processes *in vivo* make nanoparticles promising molecular imaging agents [3]. In particular, phosphorescent nanoparticles (or *nanophosphors*) are

G. Pratx, C. M. Carpenter, and C. Sun are with the Department of Radiation Oncology, Stanford University School of Medicine, Stanford, CA 94305 USA (e-mail: pratx@stanford.edu; colincarpenter@stanford.edu; conroys@stanford.edu).

*L. Xing is with Department of Radiation Oncology, Stanford University School of Medicine, Stanford, CA 94305 USA (e-mail: lei@stanford.edu).
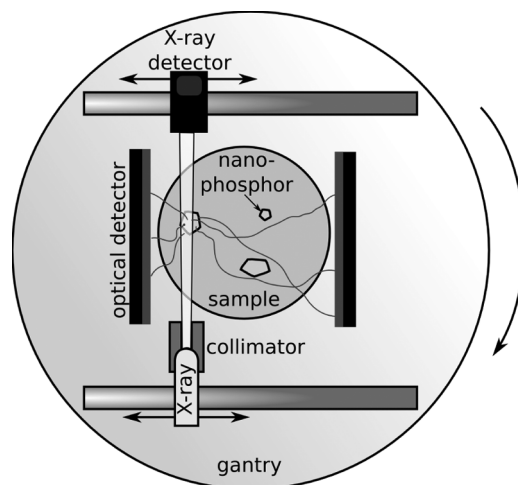
Fig. 1. Depiction of the proposed XLCT system. A computer-controlled collimated X-ray beam selectively excites the sample while photo-detectors measure the light coming out.

being investigated as possible contrast agents for up-conversion fluorescence imaging [4]–[6]. X-ray-excitable nanophosphors can also be designed and fabricated using various methods [7]–[9]. These particles are activated by high-energy electrons, such as those produced when X- and gamma-rays interact with matter through photoelectric absorption or Compton scatter. A significant advantage of using phosphors as optical molecular probes is that autofluorescence, problematic for fluorescence imaging [10] because it creates an unwanted nonspecific signal, is virtually absent in X-ray luminescence and up-conversion fluorescence. Less toxic than quantum dots [5], [11], nanophosphors can be coated with various compounds to further improve their biocompatibility [5], [12]. They are also chemically stable and resistant to photo-bleaching [5].

XLCT uses a selective excitation mechanism similar to X-ray fluorescence computed tomography (XFCT, [13]–[15]) to image samples containing unknown distributions of X-ray-excitable nanophosphor. In both schemes, the sample is irradiated by a sequence of narrow X-ray beams that are positioned at predefined locations. However, the two modalities differ in the nature of the signal produced: XFCT uses an X-ray spectrometer to measure fluorescent X-rays, while XLCT uses photo-detectors to measure the flux of optical photons diffusing out of the sample (Fig. 1).

In XLCT, it is known that measured photons were created somewhere on the narrow path of the X-ray beam; hence, the optical sensor is not required to spatially resolve photons. Because X-rays do not scatter in tissue as much as optical photons, each individual photon carries more localized information when

it is produced from such selective excitation. Therefore, high-quality tomographic images can be reconstructed even from a limited number of optical photons. In contrast, purely optical techniques, such as fluorescence molecular tomography, require many photons to solve an extremely ill-posed inverse problem, a problem made worse by the corruption of the molecular probe signal by tissue autofluorescence. [10], [16], [17].

In the proposed XLCT system, a scanning X-ray source and detector are mounted on opposite sides of the sample, in a way comparable to the first X-ray CT scanner [18]. One or more photo-detectors record the light produced in the sample. Such combination of X-ray and optical detectors enables simultaneous molecular and anatomical imaging. In addition, multiple molecular probes can be studied simultaneously because nanophosphors doped with different elements have sharp (full-width half-maximum < 20 nm) emission at different wavelengths [19]. Furthermore, we have successfully fabricated nano-sized X-ray-excitable phosphors which emit near-infrared (NIR) light, such as $Gd_2O_2S : Tm$ and $BaYF_5 : Eu^{3+}$ [20]. Such nanophosphors are well suited for *in vivo* biomedical imaging, because both X-ray and NIR photons propagate long distances in tissue [21]. In this paper, we present the results of numerical simulations, as well as a theoretical analysis of the performance of the proposed scheme.

II. THEORY

A. Imaging Model

Let us consider a sample consisting of a homogeneous material, described by its X-ray linear attenuation and energy absorption coefficients $\mu(\mathbf{r}, E)$ and $\mu_{en}(\mathbf{r}, E)$, respectively [22], where $\mathbf{r}$ is the spatial coordinate and E the X-ray energy, and by optical absorption and scattering coefficients. Nanophosphors are distributed in the sample such that their concentration in a small volume centered on $\mathbf{r}$ is $f(\mathbf{r})$. The phantom is irradiated sequentially with P different beams, while the optical signal is recorded. The kinetic energy of all the ionizing electrons liberated by the ith beam is spatially distributed according to $b_i(\mathbf{r})$, which, for a simplified monoenergetic X-ray beam model, can be expressed as

$$b_i(\mathbf{r}) = I_0 \, w_i(\mathbf{r}) \, \mu_{en}(\mathbf{r}, E) \, e^{- \int_{\mathbf{q}_i}^{\mathbf{r}} \mu(\mathbf{s}, E) ds} \qquad (1)$$

where I_0 is the beam fluence rate, $\mathbf{q}_i$ is the position of the X-ray source, and $w_i(\mathbf{r})$ is a window function, comprised between 0 and 1, which defines the geometrical aperture of the beam.

In an incremental volume $d\mathbf{r}$ centered on $\mathbf{r}$, the ith beam produces light photons at a rate $\phi_i(\mathbf{r})d\mathbf{r}$, given by rescaling the number of photons that would have been produced in the bulk crystal by the relative phosphor concentration

$$\phi_i(\mathbf{r}) = \frac{f(\mathbf{r})}{\rho_b} \, \epsilon_b \, b_i(\mathbf{r}) \qquad (2)$$

where ϵ_b and ρ_b are the light yield and the density of the bulk crystal, respectively. Over an irradiation time τ, the mean number of photons detected is

$$y_i = \tau Q_E \int_\Omega s(\mathbf{r}) \, \phi_i(\mathbf{r}) \, d\mathbf{r} + n_D \qquad (3)$$

where Q_E is the photo-detector quantum efficiency, n_D the mean dark current, Ω a volume enclosing the sample, and $s(\mathbf{r})$ the optical sensitivity map—i.e., the probability that a photon emitted at $\mathbf{r}$ will be detected by one of the photo-detectors. Because the nanophosphor is expected to be present in low concentration $(1 \ \mu g/mL)$, high-energy electrons (photo- or Compton-recoil electrons) are most likely to originate from the tissue. As the result, the photon production model does not depend upon the X-ray cross-section of the phosphor.

Using the same notations, the total kerma K_i (in Gy) quantifies the radiation dose for the ith beam

$$K_i = \tau \int_\Omega \frac{b_i(\mathbf{r})}{\rho_s} \, d\mathbf{r} \qquad (4)$$

where ρ_s is the density of the sample.

Equation (2) can be used to estimate the number of photons produced. If we assume that the light yield and density of the $Gd_2O_2S : Tm$ nanophosphor are the same as those of the bulk $Gd_2O_2S : Tb$ phosphor (i.e., $\epsilon_b = 60$ photons/keV and $\rho_b = 7.44$ g/mL, respectively [19]), irradiating a 10 mL aqueous solution of nanophosphors $(1 \ \mu g/mL)$ with a uniform X-ray dose of 1 cGy yields 5.0×10^7 photons.

B. Image Reconstruction

Maximum-likelihood (ML) reconstruction can estimate the nanophosphor concentration $f(\mathbf{r})$ based on the measurements $\mathbf{m}$. Assuming the nanophosphor distribution can be approximated using N basis functions $e_j(\mathbf{r})$, such that

$$f(\mathbf{r}) = \sum_{j=1}^{N} x_j e_j(\mathbf{r}) \qquad (5)$$

the mean number of photons measured $\mathbf{y}$ is a linear combination of the discrete tracer distribution $\mathbf{x}$

$$\mathbf{y} = A\mathbf{x}. \qquad (6)$$

The coefficients a_{ij} of the imaging matrix A satisfy

$$a_{ij} = \frac{\tau \epsilon_b}{\rho_b} s_j \int_\Omega b_i(\mathbf{r}) e_j(\mathbf{r}) d\mathbf{r} \qquad (7)$$

where s_j is the discrete approximation of the optical sensitivity map $s(\mathbf{r})$ in the basis defined by $e_j(\mathbf{r})$.

Neglecting the read noise of the photo-detectors, the noisy measurements $\mathbf{m}$ are a statistical realization of a random vector $\mathbf{Y}$, whose independent components Y_i follow a Poisson distribution with mean y_i. Hence, the log-likelihood $\log p_{\mathbf{m}}(\mathbf{y})$ given a set of noisy measurements $\mathbf{m}$ can be formulated as

$$\log p_{\mathbf{m}}(\mathbf{y}) = \sum_{i=1}^{P} -y_i + m_i \log(y_i) - \log(m_i!). \qquad (8)$$

The image $\mathbf{x}$ that satisfies the ML criterion is a solution to the convex optimization problem

$$\begin{aligned} \text{maximize} \quad & f_{\mathbf{m}}(\mathbf{y}) = \sum_{i=1}^{P} -y_i + m_i \log(y_i) \\ \text{subject to} \quad & \mathbf{y} = A\mathbf{x} \\ & \mathbf{x} \geq 0 \end{aligned} \qquad (9)$$

where the variables are $\mathbf{x} \in \mathbb{R}^N$ and $\mathbf{y} \in \mathbb{R}^P$, and the measurement vector is $\mathbf{m} \in \mathbb{R}^P$. When A is full rank, (9) has a unique solution.

In this work, we used the expectation-maximization (EM) algorithm [23] to reconstruct the data generated from the simulations. ML-EM is an iterative method which calculates successive image estimates x_j^n according to

$$x_j^{n+1} = \frac{x_j^n}{N_j} \sum_{i=1}^{P} a_{ij} \frac{m_i}{\sum_{b=1}^{N} a_{ib} x_b^n + \hat{n}_{\mathrm{D}}} \qquad (10)$$

where

$$N_j = \sum_{i=1}^{P} a_{ij} \qquad (11)$$

is a sensitivity map that takes into account the nonuniform density of the X-ray beams throughout the volumetric image, and $\hat{n}_{\mathrm{D}}$ is an estimate of the dark current, measured by acquiring a dark scan with the X-ray beam off.

Compensating for the dark current could also be attempted by precorrecting the measurements and applying the EM algorithm to $\mathbf{m} - \hat{n}_{\mathrm{D}}$. However, subtracting an estimate of the dark current alters the Poisson nature of the data, hence, it is preferable to incorporate the correction in the expectation step of the EM algorithm [24]. Scatter correction can be implemented in a similar way, provided that a scatter estimate for each projection is available.

III. METHODS

A. Simulation

A high-energy Monte-Carlo package [25] was used to calculate the distribution of ionized charges in the sample during irradiation by the X-ray beam (Fig. 2). The package simulates the interactions of high-energy photons with matter through scatter and photoelectric absorption, and, therefore, models the contribution of scattered X-rays to the total ionization. The beam width and energy were set to 1 mm and 100 keV, respectively. A single 1-mm-thick slice was irradiated from 50 radial positions, ranging from -2.5 to 2.5 cm, and 64 angles, ranging from $0°$ to $360°$. The ionization density computed from the Monte-Carlo was converted into optical light according to (2) (Fig. 2).

All the simulations assumed a cylindrical phantom, of diameter 4.5 cm, filled with tissue-mimicking material, containing various distributions of nanophosphor [Fig. 4(a)]. The nanophosphor properties were taken from those of the bulk $\mathrm{Gd_2O_2S : Tb}$ crystal, that is, a light yield of 60 photons/keV and a density of 7.44 g/mL [19]. The emission wavelength, 802 nm, was based on the emission of $\mathrm{Gd_2O_2S}$ doped with thulium. The optical absorption and scattering coefficients at 802 nm of the tissue-mimicking material were set to $0.1 \ \mathrm{cm}^{-1}$ and $100 \ \mathrm{cm}^{-1}$, respectively [26]. The density and X-ray attenuation of the material were taken for water from the NIST XCOM database [22]. It was further assumed that a ring of 2-cm-high ideal NIR detectors ($Q_{\mathrm{E}} = 1$ and $n_{\mathrm{D}} = 0$) surrounded the phantom. Based on these parameters, optical Monte-Carlo
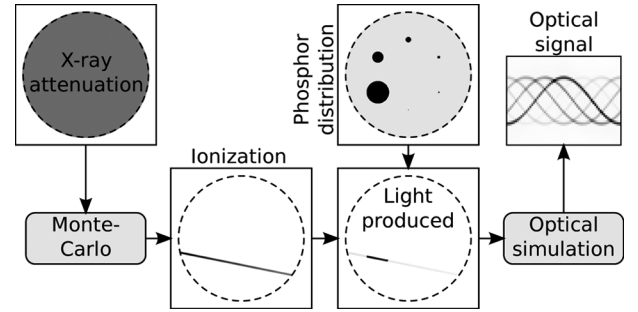

Fig. 2. Flowchart of the XLCT system simulation: The X-ray dose to the phantom is calculated by Monte-Carlo simulation using a map of the X-ray attenuation coefficients. The light produced by the nanophosphor is obtained by combining the X-ray ionization and the phosphor distribution map using (2). Finally, optical signal measured by the photo-detectors is computed from the optical sensitivity map as described in (3).
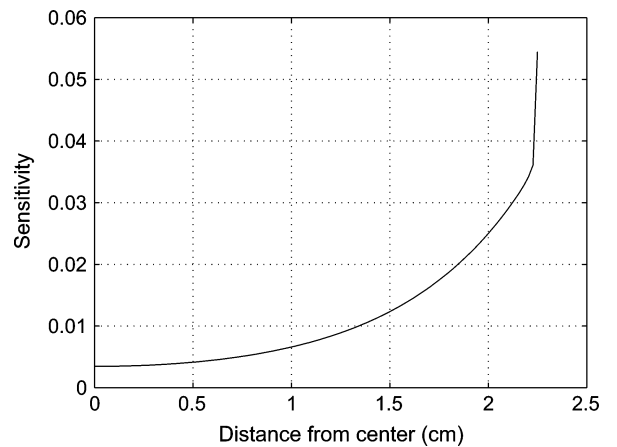

Fig. 3. Optical sensitivity of the optical detection system as a function of source position for 802 nm light.

simulations [27] were performed for computing the optical sensitivity map $s(\mathbf{r})$ (Fig. 3). The Monte-Carlo simulations were checked against the analytical solution to the diffusion equation for a point source (data not shown). In the simulation, the X-ray attenuation map, the nanophosphor distribution and the optical sensitivity map were entered as discrete 3-D arrays (voxel size 0.1 mm). For each beam position, the noise induced by limited photon counts was included by simulating a Poisson random process centered on y_i, the mean number of detected photons.

Based on these properties, a sensitivity phantom [Fig. 4(b)] was simulated to assess the minimum detectable nanophosphor distribution. Six 2-mm-diameter spheres were filled with phosphor concentrations of 0.1, 0.25, 0.5, 0.75, 1, and 2 μg/mL and included in the tissue-mimicking cylinder. No background tracer uptake was simulated. The phantom was simulated for 1, 10, and 100 cGy of total dose to tissue. A noise-free simulation was also performed (unlimited dose).

A lesion detectability phantom [Fig. 4(c)] was designed to investigate the influence of lesion size and nonspecific uptake on detectability. Six spheres, with diameter 0.25, 0.5, 1, 2, 4, and 8 mm, filled with phosphor concentrations of 1 μg/mL, were embedded in the tissue-mimicking phantom, which contained a background nanophosphor concentration of 0.1 μg/mL. Noisy
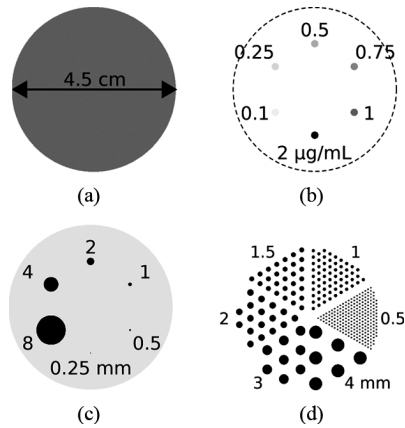
(a)   (b)   (c)   (d)

Fig. 4. Multiple nanophosphor distributions were simulated inside a (a) 4.5-cm-diameter cylinder made of tissue-mimicking material. (b) Sensitivity phantom, comprising six 2-mm-diameter spheres, filled with phosphor concentrations of 0.1, 0.25, 0.5, 0.75, 1, and 2 $\mu g/mL$. (c) Lesion detectability phantom, consisting of six spheres, of diameter 0.25, 0.5, 1, 2, 4, and 8 mm, filled with phosphor concentrations of 1 $\mu g/mL$, inside a background nanophosphor concentration of 0.1 $\mu g/mL$. (d) Spatial resolution phantom, comprising six sets of rods, of diameter 0.5, 1, 1.5, 2, 3, and 4 mm.

(1, 10, and 100 cGy of total dose to tissue) and noise-free simulations were performed.

Last, a resolution phantom [Fig. 4(d)] was studied for various beam sampling patterns. Multiple rods, of diameter 0.5, 1, 1.5, 2, 3, and 4 mm, were embedded in the tissue-mimicking phantom, with no nanophosphor background. The number of radial bins was set to either 50 or 100, and the number of angular bins was set to either 64 or 128. In order to obtain the fundamental spatial resolution limit, these experiments assumed that the dose was unlimited, hence Poisson noise was not included.

B. Reconstruction and Analysis

The X-ray transmission signal, measured with a simulated single-pixel X-ray detector, was reconstructed with filtered back-projection using a Shepp-Logan filter and 0.5 mm voxels. The nanophosphor signal was reconstructed using the ML-EM algorithm with 50 iterations. A single 2-D slice was reconstructed using 0.5 mm voxels, with system matrix coefficients computed according to (7). The reconstructed X-ray CT image was used to calculate and correct for the beam attenuation with depth. The optical sensitivity map was assumed to be known. For the sensitivity and lesion detection phantoms, the reconstructed images where smoothed with a Gaussian filter (0.8 mm full-width half-maximum).

IV. RESULTS

The X-ray transmission measurements were reconstructed with filtered back-projection [Fig. 5(a)]. Because a single-pixel X-ray detector was simulated, the spatial resolution of the X-ray CT image matches that of the optical signal. Higher spatial resolution can be achieved with a multipixel X-ray detector.

The sensitivity phantom [Fig. 4(b)] was simulated to produce a noise-free sinogram [Fig. 5(b)]. Because this phantom contains a very low amount of nanophosphor, the number of photons detected per cGy was 60.5. The sinusoidal trajectories of the six spheres are visible in the sinogram, as well as the
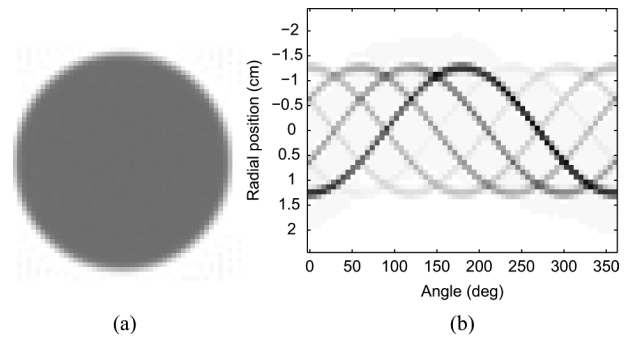

(a)   (b)

Fig. 5. (a) X-ray transmission scan reconstructed using filtered-backprojection. (b) Noise-free sinogram computed from the optical signal for the sensitivity phantom using 50 radial positions and 64 angles.

TABLE I
LINEARITY OF THE RECONSTRUCTED NANOPHOSPHOR CONCENTRATION

Dose	1 cGy	10 cGy	100 cGy	Noise-Free
R^2	0.674	0.945	0.988	0.997

X-ray scatter background. Because the X-ray beam is attenuated while traversing the sample, the sinogram is not perfectly symmetrical, which is the reason why it is preferable to scan the phantom over the full $360°$ range.

The sinogram was corrupted with Poisson noise and reconstructed with 50 iterations of the ML-EM algorithm (Fig. 6). The detectability of small spheres is determined by both radiation dose and nanophosphor concentration. For the lowest dose (1 cGy), the lowest detectable concentration is 1 $\mu g/mL$ [Fig. 6(d)]. With higher dose, lower nanophosphor concentration can be detected. For 10 cGy, sphere concentrations as low as $0.25\ \mu g/mL$ can be resolved [Fig. 6(c)]. For 100 cGy, all the spheres can be resolved. As expected, increasing the radiation dose offers a simple mechanism to resolve lower concentrations of tracer.

Increasing the dose also improves the quantitative accuracy of the reconstructed image. In the absence of noise, for the sensitivity phantom, the reconstructed concentration is proportional to the original concentration (Fig. 7). With increasing noise, the reconstructed concentration deviates from this linear relationship, as shown by the coefficient of determination (Table I).

The lesion detectability phantom [Fig. 4(c)] was simulated for various radiation doses and reconstructed with 50 iterations of ML-EM (Fig. 8). The mean number of photons produced per cGy was 1602.2. The ability to localize and quantify small lesions in a background of nonspecific uptake is affected by lesion size and radiation dose (Fig. 8). With lower radiation dose, less photons are produced and collected, therefore quantum noise is higher. Assuming a concentration of 1 $\mu g/mL$, 100 cGy of dose yields suitable image quality for 2 mm spheres; however, the image is strongly degraded when the dose is reduced to 1 cGy.

The contrast-to-noise ratio (CNR) was calculated for the different spheres, at different dose, as the ratio of the sphere contrast C_S to the background noise σ_B, which was approximated by the spatial variability (RMS) in a background ROI (Fig. 9). Lesions with CNR greater than 4 are usually detectable, even though observer experience and object shape can also affect the detectability [28]. For the noise-free simulation, all spheres
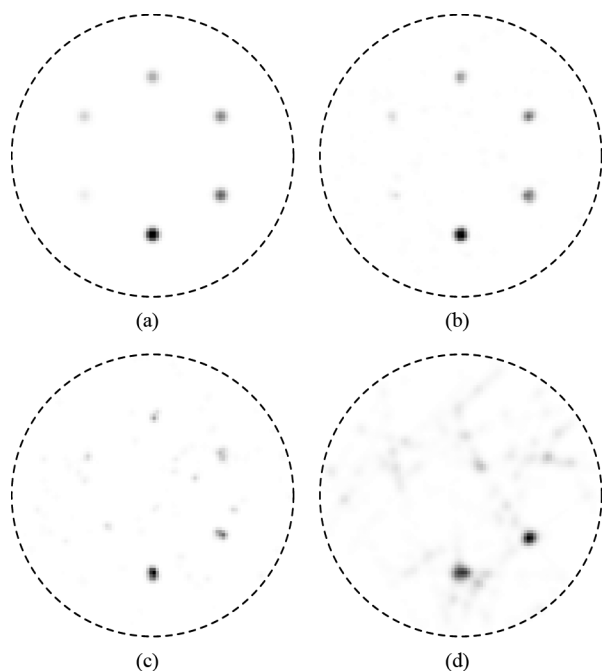
(a) (b)

(c) (d)

Fig. 6. Reconstructed images for the sensitivity phantom, which comprises six spheres of diameter 2 mm, filled with nanophosphor concentrations of 0.1, 0.25, 0.5, 0.75, 1, and 2 μg/mL, embedded in the tissue-mimicking phantom, as a function of dose: (a) Noise-free simulation (unlimited dose); (b) noisy reconstruction assuming 100, (c) 10, and (d) 1 cGy to tissue.

(a) (b)

(c) (d)

Fig. 8. Reconstructed images for the lesion detectability phantom, which comprises six spheres of diameter 0.25, 0.5, 1, 2, 4, and 8 mm, filled with phosphor concentrations of 1 μg/mL, embedded in the tissue-mimicking phantom, which contained a background nanophosphor concentration of 0.1 μg/mL, as a function of dose: (a) Noise-free simulation (unlimited dose); (b) noisy reconstruction assuming 100, (c) 10, and (d) 1 cGy to tissue.
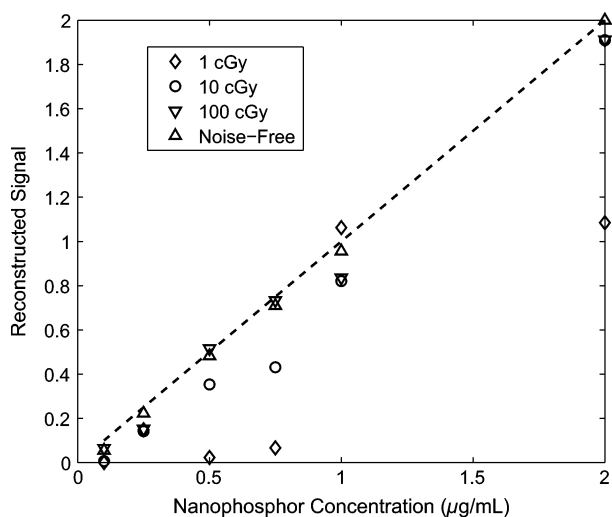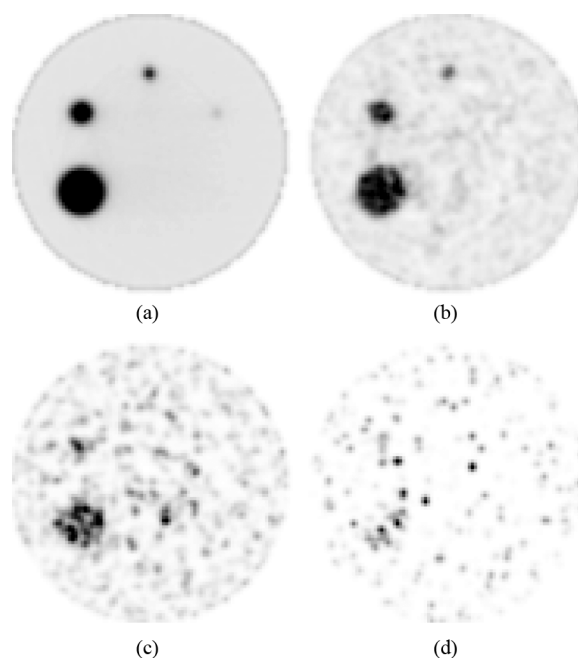

Fig. 7. Reconstructed nanophosphor concentration as a function of simulated concentration, for various levels of noise (noise-free, 1, 10, and 100 cGy). The dashed line represents the ideal concentration recovery.
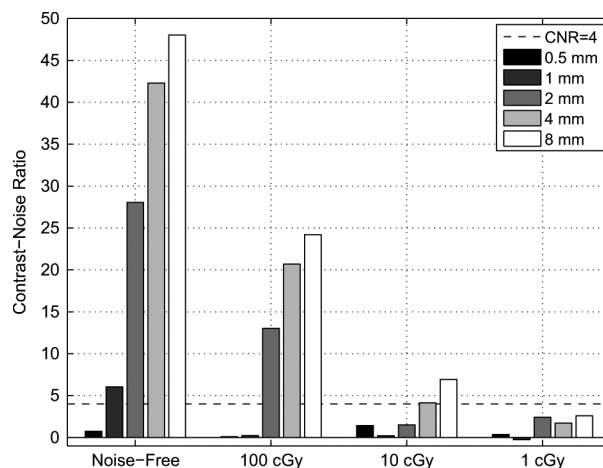

Fig. 9. Contrast-to-noise ratio (CNR), calculated as a function of sphere size and radiation dose. The dashed line represents Rose criterion [28].

larger than 1-mm-diameter can be visualized [Fig. 8(a)]. With increasing noise, it becomes more challenging to detect the smaller spheres. At 100 cGy, only the three largest spheres (2, 4, and 8 mm) are visible [Fig. 8(b)]. Additionally, the CNR of the 1 mm sphere is 0.2, compared to 6.0 for the noise-free simulation. At 10 cGy, only the two largest spheres (4 and 8 mm) are visible [Fig. 8(c)], and the CNR of the 2 mm sphere is 0.2. Because of the low phosphor concentration, at 1 cGy, the largest 8 mm sphere can hardly be resolved with the current smoothing parameters [Fig. 8(d)].

The resolution phantom [Fig. 4(d)] was simulated without noise for various sampling schemes and reconstructed with 50 iterations of ML-EM (Fig. 10). Aliasing artifacts are visible when 50 radial bins were used [Fig. 10(a) and (b)]. These artifacts disappeared with higher radial sampling [Fig. 10(c) and (d)]. Increasing the number of projection angles from 64 to 128 did not improve the spatial resolution substantially. Due to greater optical attenuation (Fig. 3), the spatial resolution is degraded at the center of the phantom. When radiation dose is not limited, the spatial resolution can be as good as 1 mm, a value consistent with the 1 mm width of the X-ray beam used in our studies.
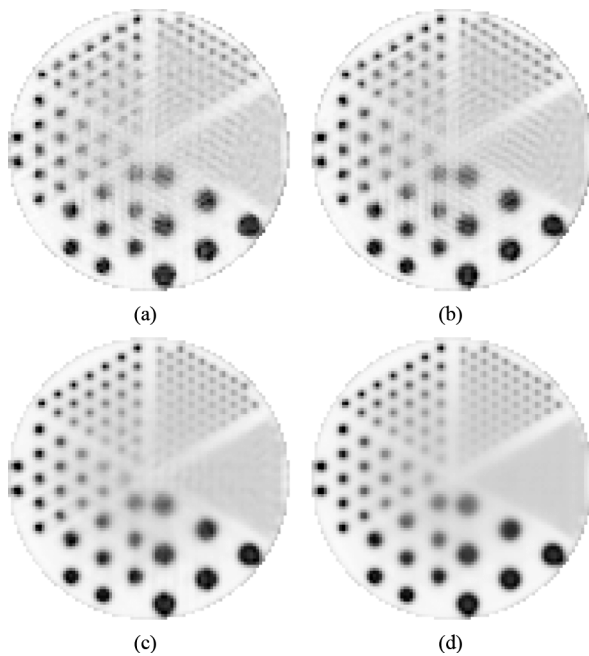
Fig. 10. Reconstructed images for the noise-free resolution phantom, which comprises multiple rods, of diameter 0.5, 1, 1.5, 2, 3, and 4 mm, embedded in the tissue-mimicking phantom, with no nanophosphor background. The projection sampling was (a) 50×64, (b) 50×128, (c) 100×64, and (d) 100×128 (angular $\times$ radial bins).

V. DISCUSSION

Based on computer simulations, we have demonstrated the feasibility of XLCT, a combined molecular and anatomical imaging modality. For a fixed concentration of X-ray-excitable NIR-emitting nanoparticles, the amount of light produced is proportional to the radiation dose to the tissue. Hence, each optical photon generated has an associated radiation dose cost. As a result, any system that attempts to use X-rays to image nanophosphors *in vivo* must be able to reconstruct high-quality images from few photons. By using a selective excitation strategy, XLCT achieves this goal. In this novel scheme, each detected photon can be positioned within the small volume of tissue covered by the beam. Hence, each photon carries far more information than if a broad irradiation was used.

From a practical standpoint, the performance of the XLCT imaging scheme is limited by the X-ray dose to the tissue, which must be kept as low as possible. For small-animal cancer imaging, high X-ray dose can affect the quantitative accuracy of longitudinal studies because of radiation side effects and unwanted therapeutic effect [29]. For clinical imaging, X-ray radiation increases the likelihood of malignancies later in life [30]. Possible variations to the method can potentially improve the SNR without increasing the dose. For example, Bayesian reconstruction, which assumes a smooth and/or sparse tracer distribution, might be able to outperform ML reconstruction. Another modification is to use imaging photo-detectors to provide further information on the source of the optical photons. When used in the reconstruction, this information should improve the image SNR without an increase in dose by offering better localization of the photon emission location. A third

option consists in irradiating the sample adaptively, delivering most of the dose in regions of interest.

The ability to detect and quantify very low concentrations of molecular tracer, known as the molecular sensitivity, is crucial in molecular imaging [31]. However, comparing very different probe systems, such as nanoparticles and small radiolabeled molecules, is a delicate exercise because the molecular sensitivity is determined both by the probe's ability to accumulate in the target while clearing from the background, and the overall performance of the imaging system. In this study, we have shown that XLCT can visualize nanoparticle concentrations in the target lower than 1 μg/mL, in the absence of nonspecific background uptake, with 1 cGy of dose (Fig. 7), a concentration that, for 50-nm-diameter nanoparticles, implies a molecular sensitivity of 0.4 pM—in the same range as other sensitive molecular imaging modality such as positron emission tomography (PET) [31].

However, a more accurate comparison of sensitivity should account for the phamacokinetics of the probe—currently under investigation for phosphor nanoparticles—and the specifics of the application. For instance, in the case of receptor imaging, probe accumulation in the target might be limited by the number of available receptors; therefore, large and re-excitable nanoparticles might provide more signal per receptor than single-decay PET probes. However, for some other applications, the mass and size of the nanoparticle can be a disadvantage, especially if cell internalization is needed. Establishing how the sensitivity of XLCT compares to other molecular imaging modalities will require application-specific investigations in small-animal disease models.

When a background of nonspecific uptake is added, high molecular sensitivity can still be achieved provided that the radiation dose is increased. Assuming a 10:1 target-to-background concentration ratio, a 2-mm-diameter lesion, containing 1 μg/mL of nanophosphor, can be clearly resolved with 100 cGy of radiation dose (Fig. 8). The same sphere requires less than 1 cGy to be detected when the nonspecific background is absent (Fig. 6).

The fundamental limit of spatial resolution is determined by the beam aperture and sampling (Fig. 10). Yet, in practice, this fundamental limit can only be achieved if the SNR is high enough. Assuming a maximum dose to the tissue of 1 cGy and an average phosphor concentration of 1 μg/mL, (2) indicates that 500 photons are produced inside a 1 mm cubic voxel. If 99% of these photons are attenuated (Fig. 3), then only five photons are recorded for every voxel in the reconstructed image, resulting in a noise level of 45%. In order to keep the noise down, the size of the voxels must be increased. Hence, to achieve a noise level of 10%, the voxel volume must be increased 20-fold, which yields a spatial resolution of 2.7 mm.

In XLCT, scattered X-rays can produce light outside the primary beam and adversely affect image quality. X-rays that interact twice (or more) in the sample produce "background" signal. However, even though more than 95% of all the interactions of the 100 keV beam with water are caused by Compton scatter [22], due to the 28 keV Compton edge, the scattered X-rays still have sufficient energy to escape the sample with high probability, without further interacting. This result was

verified by Monte-Carlo simulations: for a 5-cm-diameter water cylinder irradiated with a 1-mm-diameter, 100 keV beam, only 26% of the total ionization occurred outside the beam. Because of the relative volume of the beam and the phantom, the scattered X-rays produce a diffuse background ionization that is less than 1% of the average ionization in the beam. Therefore, for small objects, the impact of X-ray scatter on image quality is limited. Because hardware devices (such as anti-scatter grids) are not available in XLCT, X-ray scatter can only be corrected by software approaches, which can be included as part of the reconstruction process.

Knowing the optical properties of the sample is required for quantitative XLCT imaging, and a challenge in most optical imaging modalities, including fluorescence molecular tomography [16] and bioluminescence tomography [32]. In XLCT, the anatomical information obtained from X-ray transmission CT measurements can be used to help estimate the optical coefficients, for example, by using an atlas to map reference optical values to organs segmented and identified on the CT scan [32], or by using the CT scan as a prior for reconstructing a diffuse optical tomography scan [33], [34]. The optical sensitivity map can then be obtained from the optical coefficients by using the radiative transfer equation, the diffusion theory, or Monte-Carlo simulation. In practice, however, anatomical structures are complex and the accurate estimation of the optical parameters still an open research problem.

Imaging time can be a concern in the current design because the beams are acquired sequentially. As a result, high dose rates are preferable to reduce the exposure time for each beam. To further reduce the acquisition time, parallel imaging can be performed using multiple photo-detectors and multiple simultaneous excitation beams [35].

Like XLCT, XFCT uses a selective excitation mechanism [13]–[15]. In XFCT, a monochromatic X-ray beam stimulates the emission of fluorescent X-rays from elements of interest in the sample. The energy of these fluorescent X-rays is a characteristic signature of the element which emit them; therefore, using an X-ray spectrometer, it is possible to reconstruct the spatial distribution of the various elements present in the sample. In addition, XFCT can image exogenous contrast agents with high K-edge energy, such as gold nanoparticles [36]. However, the physics of the two imaging modalities differ greatly because XFCT and XLCT rely on different signal generation mechanisms, respectively, characteristic X-ray production and scintillation.

In XLCT, nanophosphors emit optical photons in response to being excited by a high-energy electron ejected during a Compton or photoelectric interaction. This optical signal can be efficiently collected using optical fibers, mirrors, and sensitive cameras. In addition, with the exception of the dark current, which can be measured and compensated, no background signal competes with X-ray luminescence. In comparison, in XFCT, only one fluorescent X-ray is emitted per photoelectric interaction and Compton interactions do not produce any signal. Furthermore, the fluorescent X-ray signal can be corrupted by a high level of background events, such as down-scatter of the primary excitation, or contamination from the X-ray fluorescence emission of other elements present in the sample or in

the room [36]. In practice, for high efficiency, XFCT requires complex instrumentation to produce precise monochromatic irradiation just above the K-edge of the element of interest, and radiation detectors with good energy resolution. These physical differences suggest that XLCT might have higher sensitivity that XFCT for detecting nanoparticles; however, gold nanoparticles can usually be injected in very large quantities [36] while the toxicity of phosphors is still under investigation.

VI. CONCLUSION

Based on computer simulations, we have demonstrated the feasibility of XLCT, a new tomographic imaging modality that provides simultaneous molecular and anatomical information. Through selective excitation with a narrow X-ray beam, XLCT can localize molecular probes with high spatial resolution, even when optical scatter in tissue is important. The spatial resolution, determined by the beam shape and sampling, can be made arbitrarily high. Furthermore, without a background of nonspecific tracer uptake, subpicomolar molecular sensitivity can be achieved for 2-mm-diameter lesions with less than 1 cGy of X-ray dose. In the presence of nonspecific tracer uptake, similarly high sensitivity can be still achieved by increasing the dose. The results of this feasibility study will be used to design and implement a prototype XLCT system for imaging small animals.

REFERENCES

[1] A. P. Alivisatos, "Semiconductor clusters, nanocrystals, and quantum dots," *Science*, vol. 271, no. 5251, pp. 933–937, 1996.

[2] S. Saini, D. D. Stark, P. F. Hahn, J. C. Bousquet, J. Introcasso, J. Wittenberg, T. J. Brady, and J. T. Ferrucci, "Ferrite particles: A superparamagnetic MR contrast agent for enhanced detection of liver carcinoma," *Radiology*, vol. 162, no. 1, pp. 217–222, 1987.

[3] W. Cai and X. Chen, "Nanoplatforms for targeted molecular imaging in living subjects," *Small*, vol. 3, no. 11, pp. 1840–1854, 2007.

[4] J. Zhou, Y. Sun, X. Du, L. Xiong, H. Hu, and F. Li, "Dual-modality in vivo imaging using rare-earth nanocrystals with NIR-to-NIR upconversion luminescence and magnetic resonance properties," *Biomaterials*, vol. 31, no. 12, pp. 3287–3295, 2010.

[5] D. K. Chatterjee, A. J. Rufaihah, and Y. Zhang, "Upconversion fluorescence imaging of cells and small animals using lanthanide doped nanocrystals," *Biomaterials*, vol. 29, no. 7, pp. 937–943, 2008.

[6] M. Nyk, R. Kumar, T. Y. Ohulchanskyy, E. J. Bergey, and P. N. Prasad, "High contrast in vitro and in vivo photoluminescence bioimaging using NIR to NIR up-conversion in $Tm3+$ and $Yb3+$ doped fluoride nanophosphors," *Nano Lett.*, vol. 8, no. 11, pp. 3834–3838, 2008.

[7] H. Wang, R. Wang, X. Sun, R. Yan, and Y. Li, "Synthesis of red-luminescent Eu^{3+}-doped lanthanides compounds hollow spheres," *Mat Res Bull*, vol. 40, no. 6, pp. 911–919, 2005.

[8] Y. Tian, W.-H. Cao, X.-X. Luo, and Y. Fu, "Preparation and luminescence property of $Gd_2O_2S : Tb$ X-ray nano-phosphors using the complex precipitation method," *J. Alloys Comp.*, vol. 433, no. 1–2, pp. 313–317, 2007.

[9] M. Xing, W. Cao, T. Pang, X. Ling, and N. Chen, "Preparation and characterization of monodisperse spherical particles of X-ray nano-phosphors based on $Gd_2O_2S : Tb$," *Chin. Sci. Bull.*, vol. 54, no. 17, pp. 2982–2986, 2009.

[10] A. Soubret and V. Ntziachristos, "Fluorescence molecular tomography in the presence of background fluorescence," *Phys. Med. Biol.*, vol. 51, no. 16, pp. 3983–4001, 2006.

[11] R. J. Palmer, J. L. Butenhoff, and J. B. Stevens, "Cytotoxicity of the rare earth metals cerium, lanthanum, and neodymium in vitro: Comparisons with cadmium in a pulmonary macrophage primary culture system," *Environ. Res.*, vol. 43, no. 1, pp. 142–156, 1987.

[12] Z. Chen, H. Chen, H. Hu, M. Yu, F. Li, Q. Zhang, Z. Zhou, T. Yi, and C. Huang, "Versatile synthesis strategy for carboxylic acid-functionalized upconverting nanophosphors as biological labels," *JACS*, vol. 461, no. 10, pp. 3023–3029, 2008.

[13] P. Boisseau, "Determination of three dimensional trace element distributions by the use of monochromatic x-ray microbeams," Ph.D. dissertation, Massachusetts Inst. Technol., Cambridge, 1986.

[14] R. Cesareo and S. Mascarenhas, "A new tomographic device based on the detection of fluorescent x-rays," *Nucl. Instrum. Methods Phys. Res.*, vol. 277, no. 2–3, pp. 669–672, 1989.

[15] P. L. Rivière and P. A. Vargas, "Monotonic penalized-likelihood image reconstruction for x-ray fluorescence computed tomography," *IEEE Trans. Med. Imag.*, vol. 25, no. 9, pp. 1117–1129, Sep. 2006.

[16] E. E. Graves, J. Ripoll, R. Weissleder, and V. Ntziachristos, "A submillimeter resolution fluorescence molecular imaging system for small animal imaging," *Med. Phys.*, vol. 30, no. 5, pp. 901–911, 2003.

[17] M. J. Eppstein, D. J. Hawrysz, A. Godavarty, and E. M. Sevick-Muraca, "Three-dimensional, Bayesian image reconstruction from sparse and noisy data sets: Near-infrared fluorescence tomography," *Proc. Nat. Acad. Sci.*, vol. 99, no. 15, pp. 9619–9624, 2002.

[18] G. N. Hounsfield, "Computerized transverse axial scanning (tomography): Part 1. Description of system," *Br. J. Radiol.*, vol. 46, no. 552, pp. 1016–1022, 1973.

[19] C. W. E. van Eijk, "Inorganic scintillators in medical imaging," *Phys. Med. Biol.*, vol. 47, no. 8, pp. R85–R106, 2002.

[20] C. Sun, C. Carpenter, G. Pratx, and L. Xing, "PEG-coated $BaYF_5$: Eu^{3+} nanophosphors for X-ray excited optical luminescence molecular imaging," in *World Molecular Imag. Congress*, 2010.

[21] C. Carpenter, G. Pratx, C. Sun, and L. Xing, "Hybrid X-ray/optical luminescence imaging: Characterization of experimental conditions," *Med. Phys.*, vol. 37, pp. 4011–4018, Aug. 2010.

[22] J. H. Hubbell, "Review of photon interaction cross section data in the medical and biological context," *Phys. Med. Biol.*, vol. 44, no. 1, p. R1, 1999.

[23] L. A. Shepp and Y. Vardi, "Maximum likelihood reconstruction for emission tomography," *IEEE Trans. Med. Imag.*, vol. 1, no. 2, pp. 113–122, Oct. 1982.

[24] A. Rahmim, J.-C. Cheng, S. Blinder, M.-L. Camborde, and V. Sossi, "Statistical dynamic image reconstruction in state-of-the-art high-resolution PET," *Phys. Med. Biol.*, vol. 50, no. 20, p. 4887, 2005.

[25] P. Olcott, S. Buss, C. Levin, G. Pratx, and C. Sramek, "Gray: High energy photon ray tracer for PET applications," in *IEEE Nucl. Sci. Symp. Conf. Rec.*, Nov. 2006, pp. 2011–2015.

[26] W. Cheong, S. Prahl, and A. Welch, "A review of the optical properties of biological tissues," *IEEE J. Quantum Electron.*, vol. 26, pp. 2166–2185, Dec. 1990.

[27] S. L. Jacques, "Light distributions from point, line and plane sources for photochemical reactions and fluorescence in turbid biological tissues," *J. Photochem. Photobiol.*, vol. 67, no. 1, pp. 23–32, 1998.

[28] A. Rose*, Vision: Human and Electronic*. New York: Plenum, 1973.

[29] J. M. Boone, O. Velazquez, and S. R. Cherry, "Small-animal X-ray dose from micro-CT," *Molecular Imag.*, vol. 3, no. 3, pp. 149–158, 2004.

[30] D. J. Brenner and E. J. Hall, "Computed tomography—An increasing source of radiation exposure," *N. Eng. J. Med.*, vol. 357, no. 22, pp. 2277–2284, 2007.

[31] C. S. Levin, "New imaging technologies to enhance the molecular sensitivity of positron emission tomography," *Proc. IEEE*, vol. 96, pp. 439–467, 2008.

[32] G. Wang, Y. Li, and M. Jiang, "Uniqueness theorems in bioluminescence tomography," *Med. Phys.*, vol. 31, no. 8, pp. 2289–2299, 2004.

[33] M. Guven, B. Yazici, X. Intes, and B. Chance, "Diffuse optical tomography with a priori anatomical information," *Phys. Med. Biol.*, vol. 50, no. 12, p. 2837, 2005.

[34] D. Hyde, R. Schulz, D. Brooks, E. Miller, and V. Ntziachristos, "Performance dependence of hybrid x-ray computed tomography/fluorescence molecular tomography on the optical forward problem," *J. Opt. Soc. Am. A*, vol. 26, no. 4, pp. 919–923, 2009.

[35] K. P. Pruessmann, M. Weiger, M. B. Scheidegger, and P. Boesiger, "SENSE: Sensitivity encoding for fast MRI," *Magn. Reson. Med.*, vol. 42, pp. 952–962, 1999.

[36] S.-K. Cheong, B. L. Jones, A. K. Siddiqi, F. Liu, N. Manohar, and S. H. Cho, "X-ray fluorescence computed tomography (XFCT) imaging of gold nanoparticle-loaded objects using 110 kVp x-rays," *Phys. Med. Biol.*, vol. 55, no. 3, p. 647, 2010.